This is an *Accepted Manuscript*, which has been through the Royal Society of Chemistry peer review process and has been accepted for publication.

Accepted Manuscripts are published online shortly after acceptance, before technical editing, formatting and proof reading. Using this free service, authors can make their results available to the community, in citable form, before we publish the edited article. We will replace this *Accepted Manuscript* with the edited and formatted *Advance Article* as soon as it is available.

You can find more information about *Accepted Manuscripts* in the **Information for Authors**.

Atomic H-induced cutting and unzipping of single-walled carbon nanotube carpets with teepee structure and their enhanced supercapacitor performance

Xiujun Fan[†‡⊥], Zhiwei Peng[‡], Yang Yang[‡], Haiqing Zhou[‡], Xia Guo[†]*

[†]College of Electronic Information and Control Engineering, Beijing University of Technology,

Beijing 100124, China

[‡]Department of Chemistry, [⊥]Richard E. Smalley Institute for Nanoscale Science and Technology,

Rice University, Houston, Texas 77005, United States

Abstract The atomic H-induced cutting and unzipping of vertically aligned single-walled carbon nanotube (VA-SWCNT) with teepee structure and vertical integrity were demonstrated. The resulting structure contains graphene nanoribbons (GNRs) and partially unzipped SWCNTs, which can be completely unzipped by changing the treated conditions. The advantage of the VA-GNR over pristine VA-SWCNT was determined by measuring the specific capacitance based on unit weight. Electrochemical characterization indicated that VA-GNRs electrodes achieved a relatively high specific capacitance of 115.7 F g^{-1} at a power density of 2.7 kW kg^{-1} and ultrahigh energy density of 105.6 Wh kg^{-1} has been measured using chronopotentiometry in 1 M TEABF$_4$ aqueous solution by cyclic voltammetry at a scan rate of 1 A s^{-1}. These values are far exceed other carbonaceous materials. The excellent rate capability of electrodes from VA-GNRs was attributed to the opening of the side-walls, shortening solid-state lengths for ionic diffusion and electronic transport, and a vertical aligned pathway, all of which facilitate the diffusion of electrolyte ions.

Key words: atomic H treatment; vertically aligned single-walled carbon nanotube (VA-SWCNT); supercapacitor; energy density; power density

Introduction

Carbon nanotubes (CNTs), particularly single-walled carbon nanotubes (SWCNTs) have exceptional electronic properties and have been proposed as replacements for silicon in applications such as low cost thin-film transistors[1-5] and high-performance logic devices[6-10]. Graphene nanoribbons (GNRs) are CNTs that have been unzipped longitudinally into ribbons, which are promising candidates for the fabrication of graphene-based nano-electronic devices because of their unique structure, versatile electronic properties, and promising applications in future carbon-based electronic devices[11, 12]. Various experimental methods have been developed to unzip CNTs (usually multi-walled CNTs) into GNRs, including wet chemistry[13], plasma etching[14, 15], catalytic cutting using microwave radiation[16, 17], lithium intercalation[18] and subsequent exfoliation[19], electronic unwrapping[20], mechanical cutting[21], and selective etching[22]. Existing methods for the production of GNRs involving the chemical synthesis cutting of graphene sheets into ribbons and ultra-sonication to exfoliate the GNRs produces low quality product[23]. Recently, the hydrogen plasma process[24-27] and the glow discharge[28] or hot tungsten wire methods[29] have been done on the reaction of SWCNTs directly with atomic H. However, there are no other reports using atomic H to unzip SWCNTs to fabricate GNRs[30]. Moreover, the CNTs materials for bulk-scale unzipping are usually in a randomly dispersed solid powder or colloidal suspension[31]. A few studies have been done on the cutting and unzipping behavior of a predefined nanotube array in a nanotube electronic device or horizontally aligned arrangement[32]. Meanwhile, VA-SWCNT carpets offer high surface area, simple growth by a well-developed chemical vapor deposition (CVD) method and good structural control by adjustment of the growth parameters. Therefore, VA-SWCNTs are potential candidates for energy storage electrodes[33, 34], field emitters[35, 36] and transparent films[37-39]. Cutting and unzipping the VA-SWCNTs while maintaining the vertically integrity of the starting material should further increase the accessible surface area, better facilitating various device fabrications[40].

As energy storage devices, electrochemical capacitors, also called supercapacitors or ultra-capacitors, have attracted much attention for use as automotive and portable energy-storage media[32]. Supercapacitors would complement batteries and regenerative energy applications due to their high capacitance, pulse power

capabilities, and long cycle life[41]. SWCNTs are candidates for electrodes in supercapacitors due to their high surface area, excellent conductivity and chemical inertness. To fabricate electrochemical supercapacitors, the VA-SWCNTs arrays would be advantageous over randomly deposited SWCNTs networks or commercially used activated carbon capacitors due to their regular pore structure and straight conductive paths that can increase the amount of interaction between the electrolyte ions and the electrode[42]. There have been limited reports regarding techniques for the post-growth manipulation of the electrical and chemical properties of SWCNTs using high-temperature gas exposure or wet chemistry[32].

Herein we demonstrate the atomic H treatment of VA-SWCNTs with preservation of vertical integrity to produce fully unzipped VA-SWCNTs (or vertically aligned graphene nanoribbons, VA-GNRs) with teepee structure. The work here combines the concept of cutting and unzipping the VA-SWCNTs carpet with an improvement in ion accessibility due to the opening of the side-walls. The large opened spaces and the aligned vertical structure not only increase the effective surface area, but also provide easily accessible paths for fast ion transport. These advantages lead to better electrochemical performance of VA-GNRs when compared to the as-prepared VA-SWCNTs in terms of the supercapacitor specific capacitance and power density.

Results and Discussion
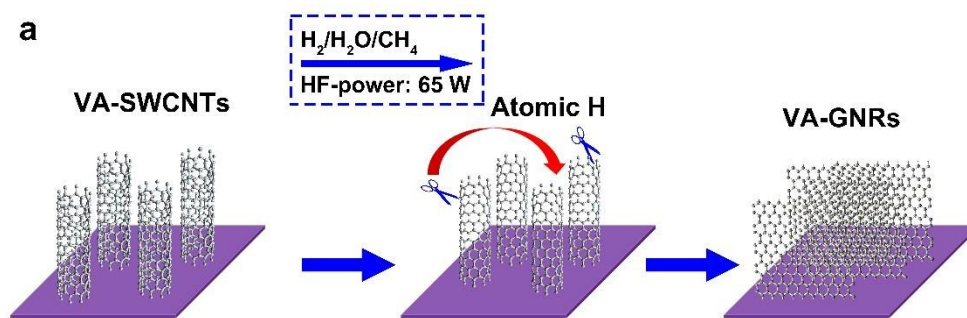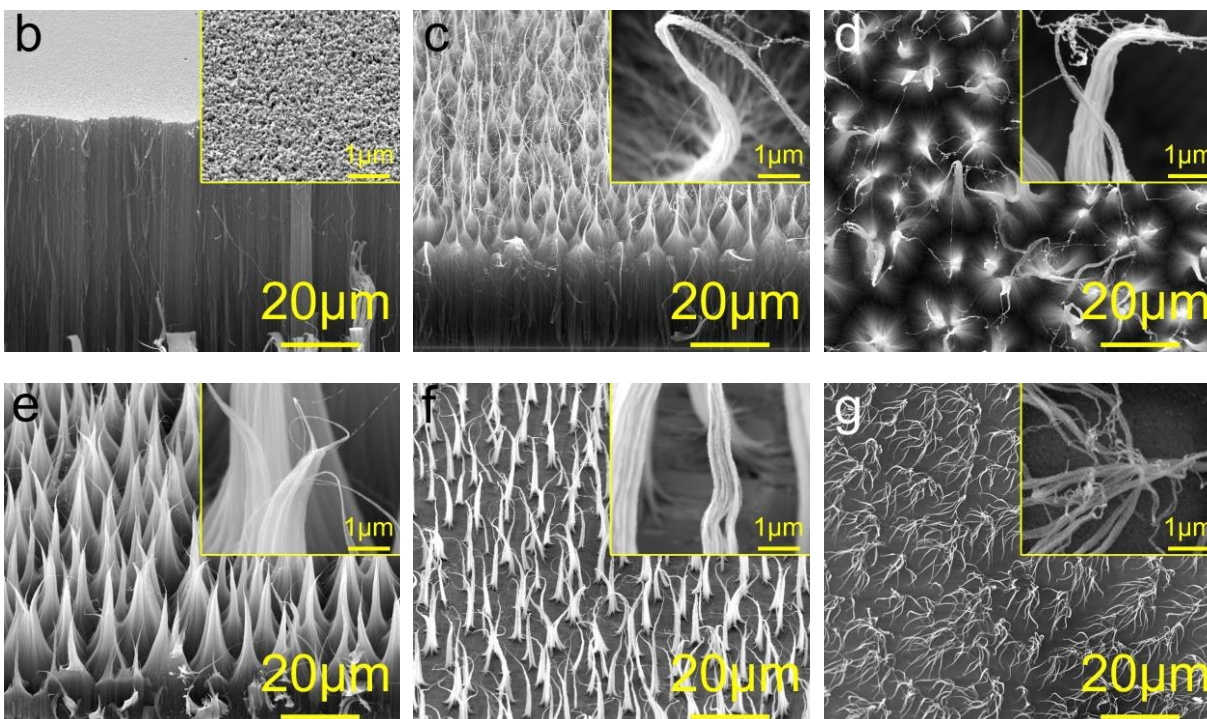
Figure 1. (a) Schematic representation of reaction involved for the atomic H treatment of VA-SWCNTs carpet. The SEM micrograph of (b) pristine and (c-d) atomic H treated VA-SWCNTs at various times and CH_4 flow rates: (c) 2 h, CH_4, 0.5 sccm; (d) 4 h, CH_4, 0.5 sccm; (e) 1 h, CH_4, 0.1 sccm; (f) 2 h, CH_4, 0.1 sccm; (g) 4 h, CH_4, 0.1 sccm.

Figure 1a is a scheme of the VA-SWCNT carpet cutting and unzipping process, during which VA-SWCNTs were firstly grown on silicon substrate according to literature[43, 44]. Next, atomic hydrogen treatment upon the samples was carried out using a mixture of H_2 (140 sccm), H_2O (15 sccm) and CH_4 (0.1-1.5 sccm) at 25 Torr and 850 ℃ for 0-4 h (for more details, see the experimental section). In the atomic H treatment process, two factors were found to be essential: treatment time, and the flow rate of the carbon feeding gas (CH_4). First, the VA-SWCNTs were treated at a constant flow rate of CH_4 (0.5 or 0.1 sccm) with various reaction time. As displayed in **Figure 1b**, the as-grown VA-SWCNT carpet has a flat surface with high density, the individual carbon nanotubes are uniformly distributed throughout the whole substrate. With atomic H treatment for 30 min, the top surface of the carpet become rougher due to surface etching with atomic H, while most nanotubes are still survived and form bundles on the top (**Figure S1a**). The space between each bundle becomes larger as the

treatment time increase (**Figure S1b**). **Figure 1c** is the SEM image of VA-GNRs treated with atomic H for 2 h; VA-SWCNTs are successfully transverse cut and longitudinal unzipped, yielding shorter fragments clumped together to meet at a point, forming a structure resembling a Native American "teepee"[45]. The diameter of the bent tails vary from several nm to 0.5 um (**Figure 1c** inset), which means the atomic H etching occurred from the top carpet to the bottom, layer by layer. The top of the VA-SWCNTs carpet is located close to the hot filament, so that the top of the arrays are neatly cut and unzipped. SEM images of the side view show that the surface became rougher with some aligned pores, which could be very beneficial for ion accessibility, fast ion diffusion and high rate-tolerant capacitance. The space between each resulting GNRs bundle become larger with treated time increased, and these ribbons form joint bundles on the top layer (**Figure 1d**). To investigate the cutting and unzipping mechanism, the VA-SWCNTs also treated with various flow rate of CH_4. **Figure 1e-g** show VA-SWCNTs treated with various time while keeping all other parameters constant, the inset in each figure shows ~~that~~ the tips of obtained VA-GNRs. Most of the SWCNTs are fully unzipped and still keep straight with teepee structure after treated for 1 h at a flow rate of 0.1 sccm (**Figure1e**). Extending the treatment time for 2 h causes most of the SWCNTs to be etched away, and the SWCNTs are fully unzipped and aggregated (**Figure 1f**). **Figure 1g** is sample treated with atomic hydrogen for 4 h, it can be found most carbon materials have been etched away, and the survived carbon nanotubes are fully unzipped with a grass-like shape. It is also worth noting that we do not observe any nanotube cutting or unzipping in the absence of a H_2. Compared with 0.5 sccm, the morphology of the VA-GNRs obtained with flow rate of CH4 at 0.1 sccm are now substantially same as the ones treated with 0.5 sccm CH_4. The tips of VA-GNRs with 0.5 sccm CH_4 are not perfectly aligned and appear distorted with some very fine particles. Under the same conditions, the resulted VA-GNRs obtained with 0.1 sccm CH_4 are greater extent cut and unzipped than those with 0.5 sccm CH_4, suggesting the atomic hydrogen produced with 0.1 sccm CH_4 is more harsh than that of 0.5 sccm. The defects generated by initial unzipping are highly active sites for further attack of atomic hydrogen, thus forming fragments. The preservation of the vertical integrity of the survived SWCNTs with a teepee structure can be attributed to the strong van der Waals interactions among the nanostructures[46].
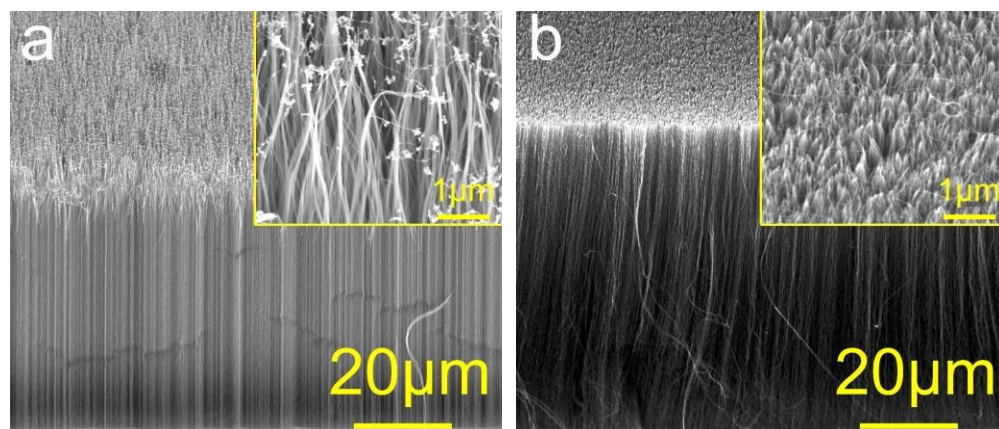
Figure 2. SEM images of the VA-SWCNTs carpets treated with atomic H for 2 h at various flow rates of CH$_4$: (a) 0.75; and (b) 1.5 sccm.

In order to examine the effect of the CH$_4$ flow rate on the atomic H treatment, the nanotube arrays were also treated with methane flow rates from 0 to 1.5 sccm at a fixed time (2 h). With the flow rate of methane at 0.75 sccm, some flower-like particles form on the top of the nanotube arrays, and the space between each nanotube bundle is small (**Figure 2a**). This indicates that, compared to the low flow rates of methane such as 0.1 or 0.5 sccm, there is still some atomic H etching with 0.75 sccm. The VA-SWCNTs carpets were also treated with higher flow rates of 1 and 1.5 sccm, and almost no atomic H etching occurred, the treated VA-SWCNTs remained a same smooth top surface (**Figure 2a, Figure S1c**). These experiments clearly show that CH$_4$ plays an important role in the atomic hydrogen etching effect on VA-SWCNTs carpets. In diamond CVD reactors, people found that hydrogen atom production decreases with increased methane concentration[47-50]. In our case, atomic hydrogen etching and cutting effects are found being very sensitivity to the flow rate of CH$_4$. **Figure S2** shows the loss of the VA-SWCNTS height as a function of the flow rate of CH$_4$. We found that the loss of the VA-SWCNTS height decreases with increasing the flow rate of CH$_4$. At high flowing rate of CH$_4$ such as above 1.0 sccm, almost no atomic H etching occurred can be attributed the etching and cut effects are suppressed due to litter atomic hydrogen is produced. At 1.0 or 1.5 sccm, a litter atomic hydrogen is generated, a weak atomic hydrogen cutting and unzipping effect is present upon the substrate, and the resulting VA-VACNT keep the same height as the initial as observed in **Figure 2b** and **Figure S1c**. While, without methane feeding, the tungsten wires used in the reaction are very easy broken. From the morphology evolution of VA-SWCNTs treated with

6

atomic hydrogen under various condition, an appropriate condition is found to be with flow rate of CH_4 at range of 0.1-0.75 sccm. Moreover, the pristine VA-SWCNTs can be considered as extremely "dirty" nanotubes contaminated with various other forms of carbon. The VA-SWCNTs subjected to atomic hydrogen treatment with a certain amount of water (15 sccm) introduced proved that, even for that kind of extremely complex carbon material, the treated samples were purified to a large extent, which is consistent with the results of TGA and XRD (**Figure S3c and d**).

TEM images of VA-GNRs with atomic H treated are shown in **Figure 3**. Contrary to the often reported rod-like cylindrical nanotubes, the VA-GNRs are flattened and twisted as shown in **Figure 3a**. Additional, thin GNRs bundles are slightly broken and some nanotube side-walls are defective (identified by arrows) in **Figure 3a**. As shown in **Figure 3b**, two nanotubes overlap and are slightly displaced parallel to the length direction, with partially opened edges, which clearly displays the unzipped layer of CNTs. It can be predicted that the cracks are generated on defect sites and the unzipping starts from these structures. Prolonging the atomic hydrogen treatment to 2 h at CH_4 flow rate of 0.5 sccm, produce the collapse and fission of individual nanoribbons, the unzipped graphene nanoribbons show in a network of high aspect ratio ribbons (**Figure 3c**). HR-TEM show that the tube are completely open, also in the majority of areas the separation between layers is approx. 3.5Å (**Figure 3d**). Carefully observed shown that the edges of obtained GNRs have more amorphous carbon than the one obtained with 1 h, which means prolonging the treatment time introduce more defect. This result is also consistent with SEM observation in **Figure 1**. While, as the flow rate of CH_4 decreased to 0.1 sccm, the GNRs obtained from unzipped VA-SWCNTs have a bundled-layer structure and straight edges, as is clearly observed in **Figure 3e-f**. The obtained GNRs show the width distribution is in a narrow range of 5 to 12 nm (**Figure S4c and d**), as defined by the VA-SWCNTs carpets starting material. These features can be explained by fully unzipping of the nanotube, which starts on the edge and goes along the length of the tube.
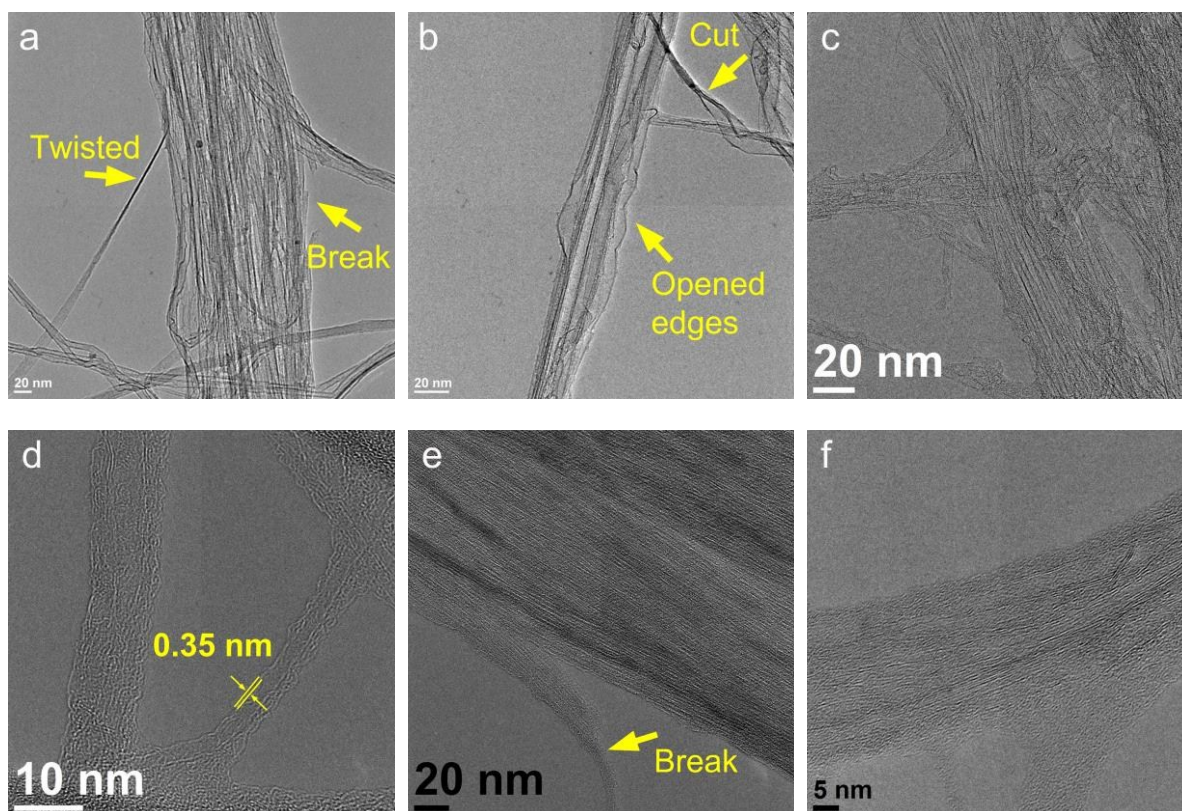
Figure 3. TEM characterizations of nanotubes from the VA-SWCNTs that had been atomic H treated, (a-b) at a CH$_4$ flow rate of 0.5 sccm for 1 h, (c-d) at a CH$_4$ flow rate of 0.5 sccm for 2 h, (e-f) at a CH$_4$ flow rate of 0.1 sccm for 2 h.

As to the atomic H-induced unzipping and cutting mechanism, we consider that the formation of GNRs might be based on the reaction between the side walls of VA-SWCNTs and highly reactive atomic hydrogen from hot filament activation. It involves reaction of VA-SWCNTs with atomic hydrogen and purification. In the reaction process, a hot filament (temperature greater than 2000 °C) is employed to create activated gas mixtures consisting of atomic hydrogen (Re. (1)) and carbon-containing species, meanwhile methane is decomposed as active carbon C (noted as C*) (Re. (2)). The newly formed gas-phase H atoms is so active that it could directly react with the side of neighboring nanotubes, breaking the C-C bonds and producing defect sites on the adjacent nanotubes[30]. The temperature of 850 °C exceeds known temperatures of C-H bond stability, and reaction of hydrogen with carbon nanotubes should proceed mostly by SWCNT cutting and etching rather than to hydrogenation of the nanotube walls[40]. So the side walls of obtained VA-GNRs contain few C-H bonds, this

8

result is consistent with the XPS result (**Figure S3b**). The two major roles of water were enhance the purification

of obtained GNRs and suppress the other carbon phase (such as nondiamond carbon, and graphitic) deposition[51,]

[52].

$$H_2 \rightarrow H^* \ (1)$$
$$CH_4 \rightarrow C^* + H^* \ (2)$$
$$H_2O \rightarrow O_2 + H^* \ (3)$$
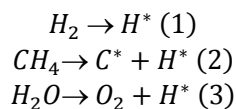
Brunauer-Emmett–Teller (BET) measurements of the VA-SWCNT carpet before and after atomic H treatment

showed that the specific surface area of the material increased from 105 to 569- 606 m^2/g. The volumetric

adsorption density jumps 5 or 6 -fold compared with the as-grown carpets. The surface area enhancement can

serve as a strong evidence for successful cutting and unzipping of VA-SWCNTs and further boost capacitive

performance. Meanwhile, the four-point probe sheet resistances of the atomic H treated VA-CNT carpets

electrodes as a function of flow rate of methane and treatment time show that sheet resistance is decreased after

atomic H treatment and keeps decreasing with the increase of methane flow rate (**Figure S5**). The expanded

inter-tube spaces, more effective surface areas and low sheet resistance could facilitate the formation of an

electrochemical double layer, thus enhancing the capacitance.
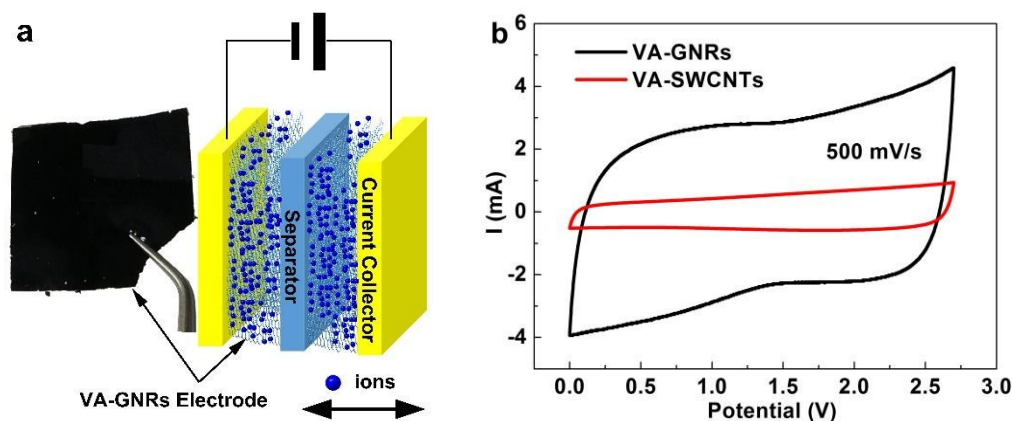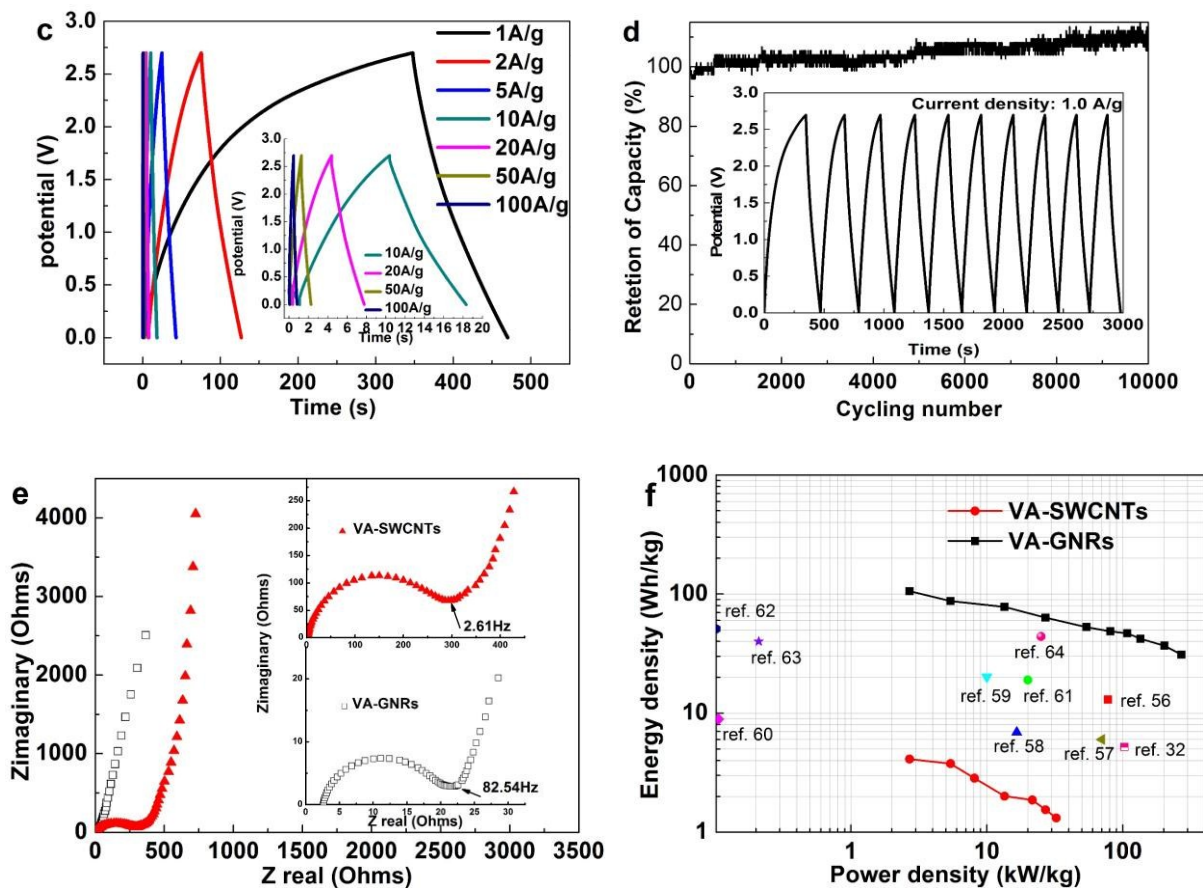
Figure 4. (a) Scheme of supercapacitor fabrication. Electrochemical characterizations of the microdevices using 1 M TEABF₄ as the electrolyte, right: photograph of a VA-GNRs film after transferred from the substrate. (b) Comparison of CV curves of the VA-SWCNT carpets and VA-GNRs measured at a scan rate of 500 mV/s. (c) separator charge/discharge curves for VA-GNRs based supercapacitor at different current densities. (d) The long-term cycling stability, inset: Galvanostatic charge-discharge curves for 10 cycles at a constant current density of 1.0 A/g of the VA-GNRs electrode. (e) Nyquist plot of the VA-GNRs electrode measured by amplitude current frequency scanning from 1,000 kHz to 0.01 Hz. A high-frequency region of the Nyquist plot is shown in the inset with its knee frequency of 82.54 Hz. (f) A Ragone plot showing the relationship between power density and energy density of the VA-SWCNTs carpet and VA-GNRs.

A schematic of the fabricated supercapacitor from the VA-GNRs film is illustrated in (**Figure 4a**). The supercapacitor device composed of stainless steel plates as current collectors (yellow), VA-GNRs film as the

electrode materials and a piece of polypropylene foil as separator (blue). 1 M Tetraethyl Ammonium Tetrafluoroborate ($TEABF_4$) solution is filled into the system as the electrolyte for the ion diffusion. Electrolyte ions are represented by the green dots. Cyclic voltammograms (CVs) were recorded at scan rates from 0.1 to 100 V s^{-1} in the potential range between 0 - 2.7 V to test the power capability of the microsystem. To demonstrate the advantages of the VA-GNRs over normal VA-SWCNTs in terms of potential applications, electrochemical supercapacitor performance tests were conducted on pristine VA-SWCNTs and the VA-GNRs to make a comparison. The VA-GNRs treated with 0.5 sccm CH_4 at 850 ^{o}C for 2 h was chosen as the VA-GNRs electrode. Unlike the direct employment of metallic substrates for growing the current collector, the free-standing VA-SWCNTs and VA-GNRs films were obtained by dissolving the substrate from the carpet using acid. This avoids a potential problem of the substrate suffering from instability in the electrolyte environment during long-term cycling. Both of VA-SWCNTs and VA-GNRs films maintained their structure and can be easily handled by tweezers, facilitating their transfer onto the backing plate of the supercapacitor device (right in **Figure 4a**). Cyclic voltammetry (CV) at a scanning rate from 10 mV to 100 V/s and a potential voltage window of 2.7 V was employed to test the VA-GNRs. As shown in **Figure 4b**, the VA-GNRs exhibit greatly enhanced electrochemical performance compared to that of pristine VA-SWCNTs. The CV curves have large enclosed area and good symmetrical rectangular shape, showing that the capacitive behavior of the device could be greatly improved with atomic H treatment. With the scan rate increased to 1 V s^{-1}, the CV curves of VA-GNRs remain rectangular at a fast scan rate, thus confirming fast charge propagation in the electrodes. The electrochemical properties are found to be stable during numbers of CV cycles, which indicates a stable delivery of ions and good connections between the VA-GNRs electrode and current collector. The discharge current densities exhibit a linear relationship with scan rate in the range of 0-10 V s^{-1} (**Figure S7**).

Galvanostatic charge/discharge curves of the symmetric cells were recorded at various current densities to further evaluate the electrochemical performance. As shown in **Figure 4c**, these typical triangular-shaped charge/discharge curves exhibit good symmetry and fairly linear slopes at different current densities, again demonstrating the ideal capacitive characteristic. The charge-discharge curves are similar in shape between 1 to 10 A g^{-1}, indicating that the supercapacitor can be stable in a wide range of current densities. The specific

capacitance of VA-GNRs cell using the discharge curve is calculated to be 115.7 Fg^{-1} at 1 Ag^{-1}, and is still maintained at 31.0 $F\,g^{-1}$ when the current density increases as much as 100 times (100 A g^{-1}). The long-term cycling stability is an important criterion for supercapacitor applications. A total of 10,000 complete charge/discharge cycles were carried out at a constant current density of 1 A g^{-1} to investigate the lifetime and durability of the VA-GNRs symmetric cell, as showed in **Figure 4d**. The VA-GNRs electrode demonstrates excellent cycle stability and a very high degree of reversibility in the repetitive charge/discharge cycling. The capacitance of VA-GNRs electrode shows a slight decrease in the initial 300 cycles, remains quite constant and then slightly increases 10% to 15% in the following cycles. The inset in **Figure 4d** represents charge/discharge curves for 10 cycles, supercapacitor shows a poor charge/discharge coulombic efficiency of ∼ 88% at first cycle. This phenomenon is consistent with the most conventional capacitor, it is partly due to the decomposition of electrolyte at the surface of electrode[53], but coulombic efficiency increase to 98% for the rest cycling tests.

Electrochemical impedance spectroscopy (EIS) analysis was used to gain insight into the resistive and capacitive behaviors of symmetric cells. The impedance spectra were analyzed by Z-SimpWin software on the basis of the electrical equivalent circuit. The resulting Nyquist plots in **Figure 4e** are composed of a spike in the low-frequency region and a semicircle in the high-frequency region. In the low-frequency region, the spike is almost a vertical line, indicating a pronounced capacitive behavior with small diffusion resistance. The VA-GNRs shows a high knee frequency of 82.54 Hz, as is shown in the inset in **Figure 4e**, which suggests that most of the stored energy is accessible even at frequencies ≥80 Hz, exhibiting a potential for applications in hybrid electrical vehicles (HEVs)[32]. At very high frequency, the x-intercept on the real axis (Z') represents a combined resistance (R_s) including intrinsic resistance of electrode materials, ionic resistance of electrolyte and contact resistance between electrode and current collector. The diameter of the semicircle corresponds to the charge-transfer resistance (R_{ct}). From the plot, it can also be seen that the R_s values are 1.97 and 2.50 Ω for symmetric cells based on the pristine VA-SWCNTs and the VA-GNRs, respectively. After atomic hydrogen treatment, the charge transfer resistance (R_{ct}) decreased from 296.2 to 19.2 Ω. The degradation of R_{ct} values is due to the feature structure of the VA-GNRs. For the CNTs electrode, the contact resistance usually comes from the interface between the CNTs and the backing plate, between the CNTs, and also the electrolyte-carbon interface when the

CNTs are assembled onto the current collector with random cross-linking between each other[32]. VA-GNRs have less contact resistance, because contact between VA-GNRs is avoided. The 45 ° sloped portion in the mediate-frequency region, known as Warburg resistance (Z_w), is a result of the frequency dependence of electrolyte diffusion/transport into the porous electrodes. From the physics aspect, this superior frequency response of VA-GNRs is due to small ESR[54] and the excellent electrolyte access and diffusion through its vertically aligned and opened-edge structured VA-GNRs electrode formed with atomic hydrogen treatment[55]. The VA-GNRs is characterized as highly homogeneous GNRs bundle structures with significant volume of open edges, thus enabling the excellent electrolyte access and diffusion. In addition, the VA-GNRs form a highly conductive film, thus reducing the internal resistance within the electrode itself. The lower internal resistance of VA-GNRs cell favors high-rate power delivery.

A Ragone plot, a performance indicator of power density against energy density, was employed to characterize the electrochemical properties of a supercapacitor cell. **Figure 4f** indicts the Ragone plots of VA-SWCNTs and VA-GNRs based symmetric supercapacitor cells. The VA-GNRs exhibit much higher power and energy densities than those of the VA-SWCNTs-based cells. More significantly, the VA-GNRs cell shows the best performance with energy density of 105.6 Wh kg^{-1} at a power density of 2.7 kW kg^{-1} and maintains a high retention of 31 Wh kg^{-1} at an ultrahigh power density of 270 kW kg^{-1}. These values are higher than other carbon based asymmetric supercapacitors reported previously[32, 56-64]. Encouragingly, the power density meets the power target of the Partnership for a New Generation of Vehicles (PNGV) [48], 15 kW kg^{-1}. The VA-GNRs not only allow the rapid delivery of the stored charge through each individual ribbon that is connected directly to the metallic backing plate, but also provide more effective accessibility for ions by unzipping the walls compared to the as-prepared VA-SWCNTs electrode, ensuing a superior power density for a capacitor.

As a result, the VA-GNRs exhibit much higher supercapacitor performance in comparison to the pristine VA-SWCNTs due to the following factors: 1) The VA-GNRs shorten solid-state lengths for ionic diffusion and electronic transport as compared to long VA-SWCNTs because of the transverse cutting. 2) The tube structure can exploit the full advantages of 1D carbon nanotube and 2D graphene structure, which eliminates the

restacking problem of graphene sheets and provides a path for rapid electron transport. 3) The longitudinal unzipping increases the effective surface area, which produces more electroactive sites for fast electrochemical reactions. Taken together, the atomic H treatment effectively improves the supercapacitor performance of carbon-based electrodes.

Conclusions

In summary, VA-SWCNTs carpets were successfully cut and unzipped with the atomic H treatment. The resulting VA-GNRs formed vertically aligned bundles with teepee structure. TEM analyses shown that the treated VA-SWCNTs contains GNRs and partially unzipped SWCNTs. Changing the treated conditions, the VA-SWCNTs can be completely unzipped. CV and galvanostatic charging-discharging measurements were performed to characterize these materials as supercapacitor electrodes. Compared to pristine VA-SWCNTs, the VA-GNRs shown much higher capacitance and had outstanding capacity retention on cycling. The VA-GNRs supercapacitor can be operated reversibly in a wide potential window as high as 2.7 V and deliver good performance, with energy density of 115.7 Wh kg^{-1} at a power density of 2.7 kW kg^{-1} and an ultrahigh power density of 105.6 kW kg^{-1}, which are much higher than those of pristine VA-SWCNTs. Furthermore, the supercapacitor exhibited long-term cycling stability with an almost 100% capacitance retention after 10,000 cycles. These results afford a convenient and efficient way to construct VA-GNRs supercapacitor based on freestanding electrode materials for the increasing demands on energy storage systems with high energy and power densities.

Acknowledgment

14

References

1.   Kang, S. J.; Kocabas, C.; Ozel, T.; Shim, M.; Pimparkar, N.; Alam, M. A.; Rotkin, S. V.; Rogers, J. A. *Nature Nanotech.* **2007,** 2, (4), 230-236.

2.   Meitl, M. A.; Zhou, Y.; Gaur, A.; Jeon, S.; Usrey, M. L.; Strano, M. S.; Rogers, J. A. *Nano Lett.* **2004,** 4, (9), 1643-1647.

3.   Kocabas, C.; Pimparkar, N.; Yesilyurt, O.; Kang, S.; Alam, M. A.; Rogers, J. *Nano Lett.* **2007,** 7, (5), 1195-1202.

4.   Wu, J.; Xie, L.; Hong, G.; Lim, H. E.; Thendie, B.; Miyata, Y.; Shinohara, H.; Dai, H. *Nano Research* **2012,** 5, (6), 388-394.

5.   Franklin, A. D.; Koswatta, S. O.; Farmer, D. B.; Smith, J. T.; Gignac, L.; Breslin, C. M.; Han, S.-J.; Tulevski, G. S.; Miyazoe, H.; Haensch, W. *Nano Lett.* **2013,** 13, (6), 2490–2495.

6.   Javey, A.; Kim, H.; Brink, M.; Wang, Q.; Ural, A.; Guo, J.; McIntyre, P.; McEuen, P.; Lundstrom, M.; Dai, H. *Nature Materials* **2002,** 1, (4), 241-246.

7.   Lefenfeld, M.; Blanchet, G.; Rogers, J. A. *Adv. Mater.* **2003,** 15, (14), 1188-1191.

8.   Sun, D.-m.; Timmermans, M. Y.; Tian, Y.; Nasibulin, A. G.; Kauppinen, E. I.; Kishimoto, S.; Mizutani, T.; Ohno, Y. *Nature Nanotech.* **2011,** 6, (3), 156-161.

9.   Cao, Q.; Han, S.-j.; Tulevski, G. S.; Zhu, Y.; Lu, D. D.; Haensch, W. *Nature Nanotech.* **2013,** 8, (3), 180-186.

10. Liu, Z.; Jiao, L.; Yao, Y.; Xian, X.; Zhang, J. *Adv. Mater.* **2010,** 22, (21), 2285-2310.

11. Li, X.; Wang, X.; Zhang, L.; Lee, S.; Dai, H. *Science* **2008,** 319, (5867), 1229.

12. Kim, K.; Choi, J.-Y.; Kim, T.; Cho, S.-H.; Chung, H.-J. *Nature* **2011,** 479, (7373), 338-344.

13. Kosynkin, D. V.; Higginbotham, A. L.; Sinitskii, A.; Lomeda, J. R.; Dimiev, A.; Price, B. K.; Tour, J. M. *Nature* **2009,** 458, (7240), 872-876.

14. Jiao, L.; Zhang, L.; Wang, X.; Diankov, G.; Dai, H. *Nature* **2009,** 458, (7240), 877-880.

15. Jiao, L.; Zhang, L.; Ding, L.; Liu, J.; Dai, H. *Nano Research* **2010,** 3, (6), 387-394.

16. Vadahanambi, S.; Jung, J.-H.; Kumar, R.; Kim, H.-J.; Oh, I.-K. *Carbon* **2013,** 53, (0), 391-398.

17. Chiu, P. L.; Mastrogiovanni, D. D. T.; Wei, D.; Louis, C.; Jeong, M.; Yu, G.; Saad, P.; Flach, C. R.; Mendelsohn, R.; Garfunkel, E.; He, H. *J. Am. Chem. Soc.* **2012,** 134, (13), 5850-5856.

18. Cano-Márquez, A. G.; Rodríguez-Macías, F. J.; Campos-Delgado, J.; Espinosa-González, C. G.; Tristán-López, F.; Ramírez-González, D.; Cullen, D. A.; Smith, D. J.; Terrones, M.; Vega-Cantú, Y. I. *Nano Lett.* **2009,** 9, (4), 1527-1533.

19. Higginbotham, A. L.; Kosynkin, D. V.; Sinitskii, A.; Sun, Z.; Tour, J. M. *ACS nano* **2010,** 4, (4), 2059-2069.

20. Kim, K.; Sussman, A.; Zettl, A. *ACS nano* **2010,** 4, (3), 1362-1366.

21. Wu, Z.-S.; Ren, W.; Gao, L.; Liu, B.; Zhao, J.; Cheng, H.-M. *Nano Research* **2010,** 3, (1), 16-22.

22. Bai, J.; Duan, X.; Huang, Y. *Nano Lett.* **2009,** 9, (5), 2083-2087.

23. Jiao, L.; Wang, X.; Diankov, G.; Wang, H.; Dai, H. *Nat Nano* **2010,** 5, (5), 321-325.

24. Hassanien, A.; Tokumoto, M.; Umek, P.; Vrbanič, D.; Mozetič, M.; Mihailović, D.; Venturini, P.; Pejovnik, S. *Nanotechnology* **2005,** 16, (2), 278.

25. Zheng, G.; Li, Q.; Jiang, K.; Zhang, X.; Chen, J.; Ren, Z.; Fan, S. *Nano Lett.* **2007,** 7, (6), 1622-1625.

26. Xie, L.; Jiao, L.; Dai, H. *J. Am. Chem. Soc.* **2010,** 132, (42), 14751-14753.

27. Sun, L. T.; Gong, J. L.; Zhu, Z. Y.; Zhu, D. Z.; Wang, Z. X.; Zhang, W.; Hu, J. G.; Li, Q. T. *Diamond Relat. Mater.* **2005,** 14, (3–7), 749-752.

28. Khare, B. N.; Meyyappan, M.; Cassell, A. M.; Nguyen, C. V.; Han, J. *Nano Lett.* **2001,** 2, (1), 73-77.

29. Kim, K. S.; Bae, D. J.; Kim, J. R.; Park, K. A.; Lim, S. C.; Kim, J. J.; Choi, W. B.; Park, C. Y.; Lee, Y. H. *Adv. Mater.* **2002,** 14, (24), 1818-1821.

30. Lu, G.; Scudder, H.; Kioussis, N. *Physical Review B* **2003,** 68, (20), 205416.

31. Wang, H.; Wang, Y.; Hu, Z.; Wang, X. *ACS Appl. Mater. Interfaces* **2012,** 4, (12), 6827-6834.

32. Zhang, C.; Peng, Z.; Lin, J.; Zhu, Y.; Ruan, G.; Hwang, C.-C.; Lu, W.; Hauge, R. H.; Tour, J. M. *ACS nano* **2013,** 7, (6), 5151-5159.

33. Izadi‑Najafabadi, A.; Yasuda, S.; Kobashi, K.; Yamada, T.; Futaba, D. N.; Hatori, H.; Yumura, M.; Iijima, S.; Hata, K. *Adv. Mater.* **2010,** 22, (35), E235-E241.

34. Izadi-Najafabadi, A.; Futaba, D. N.; Iijima, S.; Hata, K. *J. Am. Chem. Soc.* **2010,** 132, (51), 18017-18019.

35. Shimoi, N.; Estrada, A. L.; Tanaka, Y.; Tohji, K. *Carbon* **2013,** 65, 228–235.

36. Cao, Q.; Han, S.-J.; Tulevski, G. S.; Franklin, A. D.; Haensch, W. *ACS nano* **2012,** 6, (7), 6471-6477.

37. Ghosh, D.; Ghosh, P.; Yusop, M. Z.; Tanemura, M.; Hayashi, Y.; Tsuchiya, T.; Nakajima, T. *physica status solidi (RRL)-Rapid Research Letters* **2012,** 6, (7), 303-305.

38. Tyler, T. P.; Brock, R. E.; Karmel, H. J.; Marks, T. J.; Hersam, M. C. *Advanced Energy Materials* **2011,** 1, (5), 785-791.

39. Ma, R.; Menamparambath, M. M.; Nikolaev, P.; Baik, S. *Adv Mater* **2013,** 25, (18), 2548-2553.

40. Talyzin, A. V.; Luzan, S.; Anoshkin, I. V.; Nasibulin, A. G.; Jiang, H.; Kauppinen, E. I.; Mikoushkin, V. M.; Shnitov, V. V.; Marchenko, D. E.; Noréus, D. *ACS Nano* **2011,** 5, (6), 5132-5140.

41. Yuan, L.; Lu, X.-H.; Xiao, X.; Zhai, T.; Dai, J.; Zhang, F.; Hu, B.; Wang, X.; Gong, L.; Chen, J.; Hu, C.; Tong, Y.; Zhou, J.; Wang, Z. L. *ACS Nano* **2011,** 6, (1), 656-661.

42. Zhang, H.; Cao, G.; Wang, Z.; Yang, Y.; Shi, Z.; Gu, Z. *Nano Lett.* **2008,** 8, (9), 2664-2668.

43. Xu, Y.-Q.; Flor, E.; Kim, M. J.; Hamadani, B.; Schmidt, H.; Smalley, R. E.; Hauge, R. H. *J. Am. Chem. Soc.* **2006,** 128, (20), 6560-6561.

44. Pint, C. L.; Sun, Z.; Moghazy, S.; Xu, Y.-Q.; Tour, J. M.; Hauge, R. H. *ACS nano* **2011,** 5, (9), 6925-6934.

45. Zou, Y.; May, P.; Viera, S.; Fox, N. *J. Appl. Phys.* **2012,** 112, (4), 044903.

46. Choi, D. H.; Wang, Q.; Azuma, Y.; Majima, Y.; Warner, J. H.; Miyata, Y.; Shinohara, H.; Kitaura, R. *Sci. Rep.* **2013,** 3, (1617), doi:10.1038/srep01617

47. Winters, H. F.; Seki, H.; Rye, R. R.; Coltrin, M. E. *J. Appl. Phys.* **1994,** 76, (2), 1228-1243.

48. Kweon, D. W.; Lee, J. Y.; Kim, D. *J. Appl. Phys.* **1991,** 69, (12), 8329-8335.

49. Gat, R.; Angus, J. C. *J. Appl. Phys.* **1993,** 74, (10), 5981-5989.

50. Chen, K. H.; Chuang, M. C.; Penney, C. M.; Banholzer, W. F. *J. Appl. Phys.* **1992,** 71, (3), 1485-1493.

51. Larsson, K.; Björkman, H.; Hjort, K. *J. Appl. Phys.* **2001,** 90, (2), 1026-1034.

52. Matsushima, Y.; Naganuma, M.; Yamazaki, T.; Maeda, K.; Suzuki, T. *J. Appl. Phys.* **2005,** 98, 114902.

53. Wang, Y.-G.; Cheng, L.; Xia, Y.-Y. *J. Power Sources* **2006,** 153, (1), 191-196.

54. An, K. H.; Kim, W. S.; Park, Y. S.; Moon, J. M.; Bae, D. J.; Lim, S. C.; Lee, Y. S.; Lee, Y. H. *Adv. Funct. Mater.* **2001,** 11, (5), 387-392.

55. Yoon, Y.; Lee, K.; Kwon, S.; Seo, S.; Yoo, H.; Kim, S.; Shin, Y.; Park, Y.; Kim, D.; Choi, J.-Y.; Lee, H. *ACS Nano* **2014,** 8, (5), 4580-4590.

56. Sevilla, M.; Fuertes, A. B. *ACS Nano* **2014,** 8, (5), 5069-5078.

57. Wang, H.; Xu, Z.; Kohandehghan, A.; Li, Z.; Cui, K.; Tan, X.; Stephenson, T. J.; King'ondu, C. K.; Holt, C. M. B.; Olsen, B. C.; Tak, J. K.; Harfield, D.; Anyia, A. O.; Mitlin, D. *ACS Nano* **2013,** 7, (6), 5131-5141.

58. Yan, J.; Wang, Q.; Wei, T.; Jiang, L.; Zhang, M.; Jing, X.; Fan, Z. *ACS Nano* **2014,** 8, (5), 4720-4729.

59. Wu, Z.-S.; Wang, D.-W.; Ren, W.; Zhao, J.; Zhou, G.; Li, F.; Cheng, H.-M. *Adv. Funct. Mater.* **2010,** 20, (20), 3595-3602.

60. Cheng, Y.; Lu, S.; Zhang, H.; Varanasi, C. V.; Liu, J. *Nano Lett.* **2012,** 12, (8), 4206-4211.

61. Kaempgen, M.; Chan, C. K.; Ma, J.; Cui, Y.; Gruner, G. *Nano Lett.* **2009,** 9, (5), 1872-1876.

62. Fan, Z.; Yan, J.; Wei, T.; Zhi, L.; Ning, G.; Li, T.; Wei, F. *Adv. Funct. Mater.* **2011,** 21, (12), 2366-2375.

63. Chen, Z.; Augustyn, V.; Wen, J.; Zhang, Y.; Shen, M.; Dunn, B.; Lu, Y. *Adv. Mater.* **2011,** 23, (6), 791-795.

64. Choi, B. G.; Yang, M.; Hong, W. H.; Choi, J. W.; Huh, Y. S. *ACS Nano* **2012,** 6, (5), 4020-4028.

Table of Contents Graphic
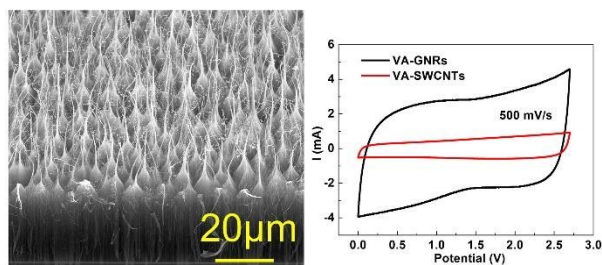
The atomic H-induced cutting and unzipping of VA-SWCNT with teepee structure and vertical integrity were

demonstrated.

20